MOLECULAR AND CELLULAR BIOLOGY, May 2007, p. 3417–3428 Vol. 27, No. 9
0270-7306/07/$08.00+0 doi:10.1128/MCB.02249-06

Molecular Insights into the Klotho-Dependent, Endocrine Mode of Action of Fibroblast Growth Factor 19 Subfamily Members[▽]

Regina Goetz,[1] Andrew Beenken,[1] Omar A. Ibrahimi,[1] Juliya Kalinina,[1] Shaun K. Olsen,[1] Anna V. Eliseenkova,[1] ChongFeng Xu,[1,7] Thomas A. Neubert,[1] Fuming Zhang,[2,7] Robert J. Linhardt,[2] Xijie Yu,[3] Kenneth E. White,[3] Takeshi Inagaki,[4] Steven A. Kliewer,[4] Masaya Yamamoto,[5] Hiroshi Kurosu,[5] Yasushi Ogawa,[5] Makoto Kuro-o,[5] Beate Lanske,[6] Mohammed S. Razzaque,[6] and Moosa Mohammadi[1]*

Department of Pharmacology[1] and Skirball Institute of Biomolecular Medicine,[7] New York University School of Medicine, New York, New York 10016; Department of Chemistry, Biology, and Chemical and Biological Engineering, Rensselaer Polytechnic Institute, Troy, New York 12180[2]; Department of Medical and Molecular Genetics, Indiana University School of Medicine, Indianapolis, Indiana 46202[3]; Department of Molecular Biology[4] and Department of Pathology,[5] The University of Texas Southwestern Medical Center at Dallas, 6000 Harry Hines Blvd., Dallas, Texas 75390; and Department of Oral and Developmental Biology, Harvard School of Dental Medicine, Boston, Massachusetts 02115[6]

Received 30 November 2006/Accepted 15 February 2007

Unique among fibroblast growth factors (FGFs), FGF19, -21, and -23 act in an endocrine fashion to regulate energy, bile acid, glucose, lipid, phosphate, and vitamin D homeostasis. These FGFs require the presence of Klotho/βKlotho in their target tissues. Here, we present the crystal structures of FGF19 alone and FGF23 in complex with sucrose octasulfate, a disaccharide chemically related to heparin. The conformation of the heparin-binding region between β strands 10 and 12 in FGF19 and FGF23 diverges completely from the common conformation adopted by paracrine-acting FGFs. A cleft between this region and the β1-β2 loop, the other heparin-binding region, precludes direct interaction between heparin/heparan sulfate and backbone atoms of FGF19/23. This reduces the heparin-binding affinity of these ligands and confers endocrine function. Klotho/βKlotho have evolved as a compensatory mechanism for the poor ability of heparin/heparan sulfate to promote binding of FGF19, -21, and -23 to their cognate receptors.

The mammalian fibroblast growth factor (FGF) family comprises 18 polypeptides (FGF1 to FGF10 and FGF16 to FGF23) which participate in a myriad of biological processes during embryogenesis, including but not limited to gastrulation, body plan formation, somitogenesis, and morphogenesis of essentially every tissue/organ such as limb, lung, brain and kidney (3, 30). FGFs execute their biological actions by binding to, dimerizing, and activating FGF receptor (FGFR) tyrosine kinases, which are encoded by four distinct genes (*Fgfr1* to *Fgfr4*). Prototypical FGFRs consist of an extracellular domain composed of three immunoglobulin-like domains, a single-pass transmembrane domain, and an intracellular domain responsible for the tyrosine kinase activity (16). The number of principal FGFRs is increased from four to seven due to a major tissue-specific alternative splicing event in the second half of the immunoglobulin-like domain 3 of FGFR1 to FGFR3, which creates epithelial lineage-specific b and mesenchymal lineage-specific c isoforms (16, 21). Generally, the receptor-binding specificity of FGFs is divided along this major alternative splicing of receptors whereby FGFRb-interacting FGFs are produced by mesenchymal cells and FGFRc-interacting FGFs are produced by epithelial cells (21). These reciprocal expression patterns of FGFs and FGFRs result in the establishment of a paracrine epithelial-mesenchymal signaling which is essential for proper organogenesis and patterning during development as well as tissue homeostasis in the adult organism.

Based on phylogeny and sequence identity, FGFs are grouped into seven subfamilies (21). The FGF core homology domain (approximately 120 amino acids long) is flanked by N- and C-terminal sequences that are highly variable in both length and primary sequence, particularly among different FGF subfamilies. The core region of FGF19 shares the highest sequence identity with FGF21 (38%) and FGF23 (36%), and therefore, these ligands are considered to form a subfamily. However, the degree of identity within the FGF19 subfamily is only 2 to 3% greater than that between FGF19 subfamily members and members of other FGF subfamilies, making this subfamily the most divergent one. FGF19 subfamily members regulate diverse physiological processes uncommon to classical FGFs, namely, energy (32) and bile acid homeostasis (FGF19) (5, 8, 13), glucose and lipid metabolism (FGF21) (10), and phosphate and vitamin D homeostasis (FGF23) (27). Moreover, unlike classical FGFs, FGF19 subfamily members achieve their unconventional activities in an endocrine fashion.

To date, only a single structure from the endocrine-acting FGF19 subfamily has been reported (4), whereas there are crystal structures available for eight classical, paracrine-acting FGFs (2, 20, 22, 37, 38, 40). The structures from the paracrine class of FGFs (FGF1, -2, -4, -7, -8, -9, -10, and -21) show that the core homology region folds into a globular domain composed of 12 antiparallel β-strands (β1 to β12) known as the

* Corresponding author. Mailing address: Department of Pharmacology, New York University School of Medicine, New York, NY 10016. Phone: (212) 263-2907. Fax: (212) 263-7133. E-mail: mohammad@saturn.med.nyu.edu.

▽ Published ahead of print on 5 March 2007.

β-trefoil motif (18). In the reported FGF19 structure (4), the region between β10 and β12 is missing, and therefore, FGF19 has only the corresponding 11 β strands, namely, β1 through β10 and β12.

Stable FGF-FGFR binding and dimerization are regulated by heparan sulfate (HS) (15), which is a polymer of variably sulfated, repeating GlcN(S)6O(S)-IdoA/GlcA(2S) disaccharide units. In all cases studied so far, HS can be replaced by heparin, which has the same disaccharide building block as HS but is more densely and uniformly sulfated along the polysaccharide chain. The crystal structure of a symmetric 2:2:2 FGF2-FGFR1c-heparin dimer has provided the molecular basis for the mechanism by which HS promotes FGF-FGFR binding and dimerization (25). Within the 2:2 FGF-FGFR dimer, the individual heparin-binding sites (HBS) of two FGFs and FGFRs are merged together and act in unison to bind specific HS sequences, leading us to propose that HS selection in FGF signaling is achieved in the context of a 2:2 FGF-FGFR dimer rather than by FGF or FGFR alone, or even by a 1:1 FGF-FGFR monomer. The heparin-binding residues of FGFs, which are generally basic, reside in the β1-β2 loop and the region encompassing the β10 strand, the β10-β11 loop, the β11 strand, and the β11-β12 loop. These solvent-exposed basic residues are in proximity to each other on the FGF β-trefoil fold and form a contiguous, positively charged surface on one side of the β-trefoil. Superimposition of the crystal structures of paracrine-acting FGFs reveals that their β10-β12 regions adopt a very similar conformation even though they differ in primary amino acid sequence.

In addition to HS, FGF19 subfamily members require Klotho/βKlotho proteins in their target tissues to exert their endocrine functions (12, 31, 33). βKlotho-deficient mice share remarkable phenotypic similarities not only with *Fgfr4* knockout mice but also with *Fgf15* knockout mice, including an increased synthesis and excretion of bile acids concomitant with activation of *CYP7A1* gene expression (9). The overlapping phenotypes strongly suggest that βKlotho may functionally interact in vivo with the FGF19-FGFR4 signaling axis to regulate bile acid homeostasis. Similarly, *Fgf23*-null mice develop phenotypes associated with premature aging (24) which resemble those seen in mice deficient in Klotho (11), indicating a cross talk between FGF23 and Klotho in vivo. Immunoprecipitation studies have shown that Klotho forms a ternary complex with FGF23 and its cognate FGFRs (12, 33).

To begin to understand the molecular basis for the Klotho-dependent, endocrine mode of action of FGF19 subfamily members, we determined the crystal structures of FGF19 alone and of FGF23 in complex with sucrose octasulfate (SOS), a disaccharide chemically related to heparin. We show that the heparin-binding regions of FGF19 and FGF23 adopt unique conformations that translate into poor binding affinity for HS/heparin and hence the endocrine mode of action of these ligands. The poor heparin-binding affinity of FGF19 subfamily members restricts signaling of these ligands to tissues expressing Klotho/βKlotho proteins. Klotho/βKlotho partially make up for the poor ability of HS/heparin to promote FGF19/21/23-FGFR binding and dimerization by interacting concomitantly with ligand and receptor and enhancing their binding affinity.

MATERIALS AND METHODS

Purification and crystallization of FGF19 and FGF23 proteins. Human FGF19 and FGF23 proteins were expressed in *Escherichia coli*, refolded in vitro, and purified by previously published protocols (6, 23). Crystals of FGF19 and the FGF23 core domain were grown by hanging-drop vapor diffusion. The FGF19 protein was concentrated to ~12 mg ml^{-1} in 25 mM HEPES-NaOH (pH 7.5), 417 mM NaCl, and the FGF23 protein was concentrated to 3.71 mg ml^{-1} in 25 mM HEPES-NaOH (pH 7.5), 150 mM NaCl, 50 mM $(NH_4)_2SO_4$, 205 mM imidazole, 25 mM SOS. Concentrated protein was mixed 1:1 with reservoir solution and equilibrated against 750 μl of reservoir solution at 20°C. FGF19 crystallized under three sets of crystallization conditions: (i) 100 mM trisodium citrate (pH 5.75) and 14% (vol/vol) polyethylene glycol 1000; (ii) 85 mM sodium cacodylate (pH 6.5), 170 mM $(NH_4)_2SO_4$, 25.5% (vol/vol) polyethylene glycol 8000, and 15% (vol/vol) glycerol; and (iii) 100 mM Tris-HCl (pH 8.5), 200 mM sodium acetate, and 15% (vol/vol) polyethylene glycol 4000. FGF23 crystals were grown over a reservoir of 100 mM Tris-HCl (pH 8.5), 1.0 M $(NH_4)_2SO_4$, and 10 mM $[Co(NH_3)_6]Cl_3$. Cryoprotection was achieved by soaking crystals in the reservoir solution supplemented with 20 to 25% (vol/vol) glycerol before flash freezing under a liquid nitrogen stream. Diffraction data were collected and processed for each of the three FGF19 crystals. All FGF19 crystals were of space group P3 and contained two FGF19 molecules in the asymmetric unit. The data collected for FGF19 crystals grown over a reservoir of 100 mM trisodium citrate (pH 5.75) and 14% (vol/vol) polyethylene glycol 1000 were used for structure determination. The unit cell dimensions of these crystals are as follows: $a = 67.36$ Å, $b = 67.36$ Å, and $c = 54.64$ Å. FGF23 crystals were of space group $P2_12_12_1$, with unit cell dimensions as follows: $a = 38.81$ Å, $b = 47.09$ Å, and $c = 84.93$ Å. These crystals contained one FGF23 molecule in the asymmetric unit.

X-ray diffraction data collection and structure determination. Diffraction data were collected at the National Synchrotron Light Source beam line X4A, and data sets were indexed, integrated, and scaled using DENZO and SCALEPACK. The FGF19 structure was determined by molecular replacement using the program AMoRe and the published FGF19 structure (Protein Database identification [PDB ID], 1PWA) (4) as the search model. The FGF23 structure was also solved by molecular replacement, with our FGF19 structure minus the β10-β12 region as the search model. Models were built into $2F_o$-F_c and F_o-F_c electron density maps using program O and refined with the CNS suite. The final model for the FGF19 structure contains residues Asp40 to Glu175 of two FGF19 molecules; residues 23 to 39 at the N terminus and 176 to 216 at the C terminus are disordered in each of the two molecules. The final FGF23 model contains residues Ser29 to Asn170; the N-terminal residues 25 to 28 and the C-terminal residues 171 to 179 are disordered. Analysis of FGF23 crystals by MALDI-TOF (matrix-assisted laser desorption ionization–time of flight) mass spectrometry (TofSpec 2E; Micromass/Waters) revealed that the N-terminal hexahistidine tag had been cleaved from the protein in the course of crystallization.

SPR analysis of FGF19/21/23-heparin binding. Binding of FGF19, -21, and -23 to heparin was analyzed by surface plasmon resonance (SPR) spectroscopy by a previously reported protocol (7). A heparin sensor chip was prepared by immobilizing biotinylated heparin on a research-grade streptavidin chip (Biacore AB, Uppsala, Sweden). Increasing concentrations of FGF19, FGF21, or FGF23 in HBS-EP buffer (10 mM HEPES-NaOH [pH 7.4], 150 mM NaCl, 3 mM EDTA, 0.005% [vol/vol] polysorbate 20) were injected over the neoproteoglycan chip at a flow rate of 50 μl min^{-1}. At the end of each FGF injection (180 s), HBS-EP buffer (50 μl min^{-1}) was passed over the chip to monitor dissociation for 180 s. The chip surface was then regenerated by injecting 50 μl of 2.0 M NaCl in 10 mM sodium acetate (pH 4.5). The data were processed with BiaEvaluation software (Biacore AB). For each FGF injection, responses from the control flow cell (due to nonspecific binding to streptavidin) were subtracted from the responses recorded for the heparin flow cell. The sensorgrams were then used to determine kinetic parameters by globally fitting the entire association and dissociation phases to a 1:1 interaction as previously described (7). Finally, the sensorgrams were manually examined for accuracy of the model fit. χ^2 was less than 10% of R_{max} for each fit. For comparison, heparin binding was also determined for FGF1, FGF2, FGF4, FGF7, and FGF10. Additionally, HBS mutants of FGF19 and FGF23 were analyzed.

Analysis of *CYP7A1* gene expression in mice in response to FGF19. In primary cultures of human hepatocytes, FGF19 was shown to downregulate expression of the gene encoding cholesterol 7α-hydroxylase (CYP7A1), an enzyme which catalyzes the first and rate-limiting step in bile acid synthesis (5). To assess biological activity of our recombinant FGF19 protein in vivo, we analyzed its effect on *CYP7A1* gene expression. FGF19 protein (1.3 to 333.3 μg kg body $weight^{-1}$) or vehicle (isotonic saline) was injected into the jugular veins of wild-type mice. At 6 h after injection, the mice were killed, and liver tissue was

excised and flash-frozen in liquid nitrogen. Total RNA was isolated from liver tissue, and CYP7A1 mRNA levels were determined by quantitative real-time reverse transcription (RT)-PCR as previously described (8). Cyclophilin was used as internal standard. All animal care and experiments were approved by the Animal Care and Research Advisory Committee at the University of Texas Southwestern Medical Center and complied with the *Guide for the Care and Use of Laboratory Animals* (19).

Determination of serum phosphate levels in mice in response to FGF23. Recombinant FGF23 proteins or vehicle (25 mM HEPES-NaOH [pH 7.5], 1.0 M NaCl) was injected intraperitoneally into *Fgf23* knockout mice (29). Each animal received two injections at 8-h intervals and 5 μg of protein per injection. Before the first injection and 8 h after the second injection, blood was drawn from the tail vein and spun at 3,000 × *g* for 10 min to obtain serum. Blood samples were also taken from wild-type mice not receiving any protein injection. Serum phosphate levels were determined colorimetrically using the Phosphorus Liqui-UV reagent (Stanbio Laboratory). All animal care and experiments were approved by the Harvard University Animal Care and Research Committee and complied with the *Guide for the Care and Use of Laboratory Animals* (19).

Analysis of EGR1 mRNA expression in response to FGF23. To assess biological activity of our FGF23 proteins at the cellular level, we studied the ability of these proteins to activate *early growth response 1* (*EGR1*) gene expression, FGFR substrate 2α (FRS2α), and 44/42 MAP kinase, all of which can serve as a tool to measure FGFR activation. For these studies, we used human embryonic kidney 293 (HEK293) cells, which endogenously express at least three of the four FGF23 cognate receptors, namely, FGFR1c, FGFR2c, and FGFR3c (12). HEK293 cells transiently transfected with the full-length transmembrane isoform of Klotho were starved with serum-free DMEM/F12 medium plus 0.2% bovine serum albumin for 24 h and then stimulated with FGF23 proteins (1 ng ml^{-1}) for 30 min. After stimulation, total RNA was extracted from the cells, and EGR1 mRNA levels were determined by quantitative real-time RT-PCR using β-actin as the internal standard. The primers and probes used for EGR1 were 5′-GGA CACGGGCGAGCAG-3′, 5′-CGTTGTTCAGAGAGATGTCAGGA-3′, and 5′-CCTACGAGCACCTGACCGCAGAGTCT-3′; the primers and probes for β-actin were 5′-GGCACCCAGCACAATGAAG-3′, 5′-GCCGATCCACACGG AGTACT-3′, and 5′-TCAAGATCATTGCTCCTCCTGAGCGC-3′. Each RNA sample was analyzed in triplicate on an ABI-PRISM 7700 sequence detection system (Applied Biosystems), and relative mRNA levels were calculated using the comparative cycle threshold method.

Analysis of phosphorylation of FRS2α and 44/42 MAP kinase in response to FGF19 and FGF23. Subconfluent cells of a HEK293 cell line stably expressing the full-length transmembrane isoform of Klotho (12) were serum starved for 16 h and then stimulated with recombinant FGF23 proteins (3 to 3,000 pM) for 10 min. Similarly, subconfluent cells of the H4IIE hepatoma cell line, which endogenously expresses βKlotho, were treated with recombinant FGF19 protein. After stimulation, the cells were snap-frozen in liquid nitrogen and lysed (12), and total cellular proteins were resolved on sodium dodecyl sulfate (SDS)-polyacrylamide gels and transferred to nitrocellulose membranes. The protein blots were probed with antibodies to phosphorylated FRS2α and phosphorylated 44/42 MAP kinase. Antibodies to Klotho and nonphosphorylated 44/42 MAP kinase were used to control for even expression of Klotho and 44/42 MAP kinase proteins among the cell samples. Except for the anti-Klotho antibody, which was developed in the Tokyo Research Laboratories, all antibodies were from Cell Signaling Technology.

Analysis of FGF23 binding to Klotho. Subconfluent cells of a HEK293 cell line stably expressing the full-length transmembrane isoform of Klotho (12) were lysed in 25 mM HEPES buffer (pH 7.5) containing 150 mM NaCl, 1 mM EDTA, 20 mM CHAPS (3-[(3-cholamidopropyl)-dimethylammonio]-1-propanesulfonate), and protease inhibitors. Recombinant FGF23 proteins (10 μg per p150 dish of lysed cells) and anti-FLAG M2 agarose (Sigma-Aldrich) were added to the cell lysate, and the samples were incubated for 2 h at 4°C. FGF21 protein was used as a negative control. Agarose beads were collected and washed four times with 25 mM HEPES buffer (pH 7.5) containing 150 mM NaCl, 1 mM EDTA, and 12 mM CHAPS. Bead-bound proteins were resolved on 12% SDS–polyacrylamide gels, and the gels were stained with Coomassie brilliant blue.

Statistical analysis. Unless stated otherwise, data are presented as means ± standard errors of the means and were analyzed by the Tukey-Kramer test. Differences were considered statistically significant when P was less than 0.01.

Protein structure accession numbers. The atomic coordinates and structure factors have been deposited into the RSCB Protein Data Bank at http://www.rscb.org/pdb/ with accession numbers PDB 1D, 2P23 (FGF19), and 2P39 (FGF23).

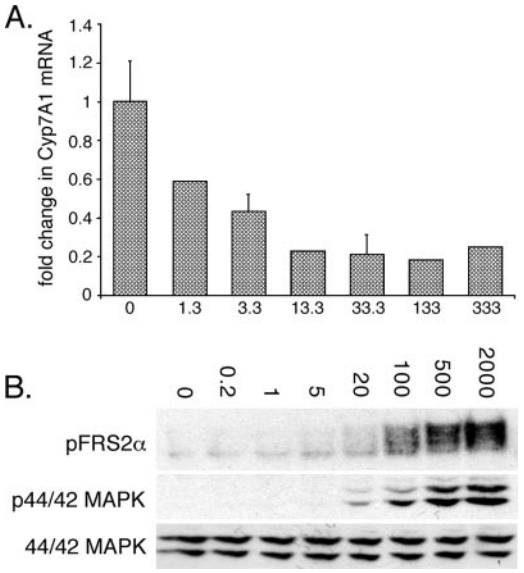

FIG. 1. Recombinant FGF19 protein is biologically active. (A) Repression of *Cyp7a1* by FGF19. FGF19 (1.3 to 333.3 μg kg body $weight^{-1}$) was injected intravenously into mice, and CYP7A1 mRNA levels were measured by real-time RT-PCR using total RNA isolated from liver tissue. The data are presented as the change in CYP7A1 mRNA level. (B) Activation of FRS2α and MAP kinase cascade by FGF19. H4IIE hepatoma cells were stimulated with FGF19 (0.2 ng ml^{-1} to 2 μg ml^{-1}; numbers above the lanes show amounts in ng ml^{-1}) for 10 min, and cell lysate was prepared and analyzed for phosphorylation of FRS2α (pFRS2α) and 44/42 MAP kinase (p44/42 MAPK) by immunoblotting. Total protein expression of 44/42 MAP kinase was measured to confirm even expression among the cell samples.

RESULTS AND DISCUSSION

The topology of the HBS of FGF19 differs completely from that of paracrine-acting FGFs. We first confirmed the biological activity of our recombinant human FGF19 protein both in mice and in cultured cells. Increasing concentrations of FGF19 protein were injected intravenously into mice, and liver CYP7A1 gene expression was analyzed. FGF19 reduced CYP7A1 mRNA levels in a dose-dependent fashion (Fig. 1A). In parallel, we stimulated H4IIE hepatoma cells with FGF19 and analyzed activation of FRS2α and of the MAP kinase cascade. FGF19 robustly induced phosphorylation of FRS2α, the direct substrate of FGFRs, and 44/42 MAP kinase (Fig. 1B). These data confirmed that our FGF19 ligand is biologically active.

FGF19 was crystallized under three different sets of crystallization conditions (see Materials and Methods), all yielding hexagonal crystals of space group P3 with two FGF19 molecules per asymmetric unit. We solved our crystal structure of FGF19 by molecular replacement using the previously published FGF19 crystal structure (PDB ID, 1PWA) (4) as the search model. In this structure, the major heparin-binding region between β10 and β12 could not be resolved due to the lack of interpretable electron density. Analysis of the F_o-F_c difference map calculated using the search model revealed clear and strong electron density for the missing β10-β12 region in both copies of FGF19 in the asymmetric unit of our crystals. Our FGF19 structure has been refined to a 1.8-Å

TABLE 1. Data collection statistics from crystallographic analysis

Protein	Resolution (Å)	Reflections (total/unique)	Completeness (%)[a]	R_{sym} (%)[a,b]	Signal ($\langle I/\sigma I \rangle$)
FGF19	50–1.8	117,476/25,585	99.9 (99.9)	5.0 (34.3)	25.6
$FGF23^{core}$	50–1.5	305,261/25,550	99.5 (95.6)	5.9 (29.7)	26.1

[a] Values in parentheses are for the highest-resolution shell: 2.07 to 1.8 Å (FGF19) and 1.55 to 1.5 Å ($FGF23^{core}$).
[b] Calculated as $100 \times \Sigma_{hkl}\Sigma_i|I_i(hkl) - \langle I(hkl)\rangle|/\Sigma_{hkl}\Sigma_i I_i(hkl)$.

TABLE 2. Refinement statistics from crystallographic analysis[a]

Protein	Resolution (Å)	Reflection	R_{cryst}/R_{free} (%)[b]	Root-mean-square deviations		
				Bond (Å)	Angle (°)	B factor ($Å^2$)[c]
FGF19	25–1.8	25,259	25.1/28.5	0.006	1.3	1.1
$FGF23^{core}$	25–1.5	25,152	20.3/21.4	0.006	1.4	1.5

[a] Atomic model: 2,092 protein atoms (FGF19), 1,113 protein atoms ($FGF23^{core}$), 55 SOS atoms, and 98 (FGF19) and 93 (FGF23) water molecules.
[b] Calculated as $100 \times \Sigma_{hkl}\|F_o(hkl)| - |F_C(hkl)\|/\Sigma_{hkl}|F_o(hkl)|$, where F_o (>0) and F_c are the observed and calculated structure factors, respectively. 10% of the reflections were used for calculation of R_{free}.
[c] For bonded protein atoms.

resolution with working and free *R* values of 24.2% and 25.9%, respectively (Tables 1 and 2), and the final model consists of two copies of FGF19 residues 40 to 176 (Fig. 2A).

The conformation of the segment between β10 and β12 in our FGF19 structure is completely different from the common conformation adopted by paracrine-acting FGFs (Fig. 2B and C). The Cα path of FGF19 starts to diverge from the common path adopted by these FGFs at Leu145 and converges again with these FGFs at Leu162, three residues before the β12 strand (Fig. 2B and 3B). Residues Lys149 to Lys155 in this region of FGF19 adopt a helical conformation, whereas paracrine-acting FGFs have the canonical β11 strand. This helix in FGF19, which we have termed α11 to reflect the lack of β11, bulges out of the rest of the protein fold, which has the corresponding 11 β strands, namely, β1 through β10 and β12 (Fig. 2A and 3A). The presence of the α11 helix in this segment gives FGF19 an atypical trefoil appearance.

Superimposition of the 11 structurally homologous β strands between FGF19 and other FGF structures shows that the conformation of the β1-β2 loop of FGF19, the other major heparin-binding region, is also substantially different from that of other FGFs (Fig. 2B). This loop, which is the longest among all FGFs, also stretches out of the β-trefoil like core region of FGF19 at the same side of the trefoil where the α11 helix is located (Fig. 2A and 3A). Due to the protrusion of both heparin-binding regions, the HBS of FGF19 is lifted atop of the remaining β-trefoil like domain and thus appears structurally separated from the rest of FGF19 (Fig. 2A). This is in stark contrast to all other FGFs, where the heparin-binding regions are structurally integrated into the β-trefoil core domain as they directly participate in the folding of the β-trefoil. The HBS of FGF19 distinguishes itself further from that of paracrine-acting FGFs by the presence of a cleft between the β1-β2 loop and β10-β12 region (Fig. 2A). The formation of this cleft is due to the fact that in FGF19, there are no intramolecular interactions between these two heparin-binding elements (Fig. 2B).

The divergent conformation of the region between β10 and β12 observed in our crystal structure is not biased by crystal packing forces for several reasons. Firstly, this region is missing in 1PWA, the search model used for solving our FGF19 structure. Secondly, we obtained the same structure from crystals grown in different crystallization buffers (see Materials and Methods). Thirdly, the conformation of this region is virtually indistinguishable between the two independent copies of FGF19 in the asymmetric unit of our crystals; since the two FGF19 molecules experience different lattice contacts in the crystal, the observed conformation/ordering of this region cannot be biased by crystal packing forces. Fourthly, even algorithms such as AGADIR, used to assess the helical propensity of short peptides, predict an α helix at precisely the same location within the segment between β10 and β12 as observed in our FGF19 crystal structure. Lastly, reanalysis of 1PWA in light of our FGF19 structure shows that even in 1PWA, the Cα positions of Ser147 and Phe159 at either end of the disordered region have already begun to diverge from the Cα backbone of paracrine-acting FGFs and point towards the α helix seen in our FGF19 crystal structure.

The topology of the HBS of FGF23 also differs completely from that of paracrine-acting FGFs. FGF23 circulates in the bloodstream in two distinct forms: a full-length mature form (Tyr25-Ile252; $FGF23^{wt}$) and a shorter form (Tyr25-Arg179; $FGF23^{core}$) lacking the unique 73-amino-acid C-terminal tail (1, 36). The shorter form arises from proteolytic cleavage at the $^{176}RXXR^{179}$ site, which follows the predicted FGF core homology region of FGF23 (28, 35). Mutations at either of the two Arg residues result in accumulation of circulating full-length FGF23, which signals in the kidney to cause phosphate wasting in patients with autosomal-dominant hypophosphatemic rickets (ADHR) (34). Since ADHR is inherited in an autosomal dominant fashion, it has been postulated that the C-terminal tail of FGF23 is required for regulation of phosphate homeostasis by this FGF (28, 35).

We expressed and purified $FGF23^{wt}$, $FGF23^{core}$, and $FGF23^{ADHR}$, an FGF23 protein harboring ADHR mutations, and assessed their biological activity in mice and in cultured cells. Both $FGF23^{wt}$ and $FGF23^{ADHR}$ reduced serum phosphate to near-normal levels in *Fgf23*-null mice, whereas $FGF23^{core}$ had no statistically significant effect (Fig. 4A). In HEK293 cells overexpressing Klotho, both $FGF23^{wt}$ and $FGF23^{ADHR}$ robustly induced EGR1 gene expression, whereas $FGF23^{core}$ had almost no activity (Fig. 4B). Similarly, both $FGF23^{wt}$ and $FGF23^{ADHR}$ robustly activated FRS2α and 44/42 MAP kinase, whereas $FGF23^{core}$ failed to induce phosphorylation of these downstream mediators of FGF signaling (Fig. 4C). These data provide the first evidence that FGF23 requires its C terminus to signal. To gain insights into the molecular basis for this requirement, we compared the ability of $FGF23^{wt}$ and $FGF23^{core}$ to bind Klotho. Coimmunoprecipitation studies showed that $FGF23^{core}$ failed to bind Klotho, indicating the involvement of the C-terminal tail of FGF23 in the interaction of $FGF23^{wt}$ with Klotho (Fig. 4D). These data suggest that Klotho proteins interact simultaneously with the C-terminal tail of FGF23 and an unknown region of FGFR to enhance ligand-receptor affinity.

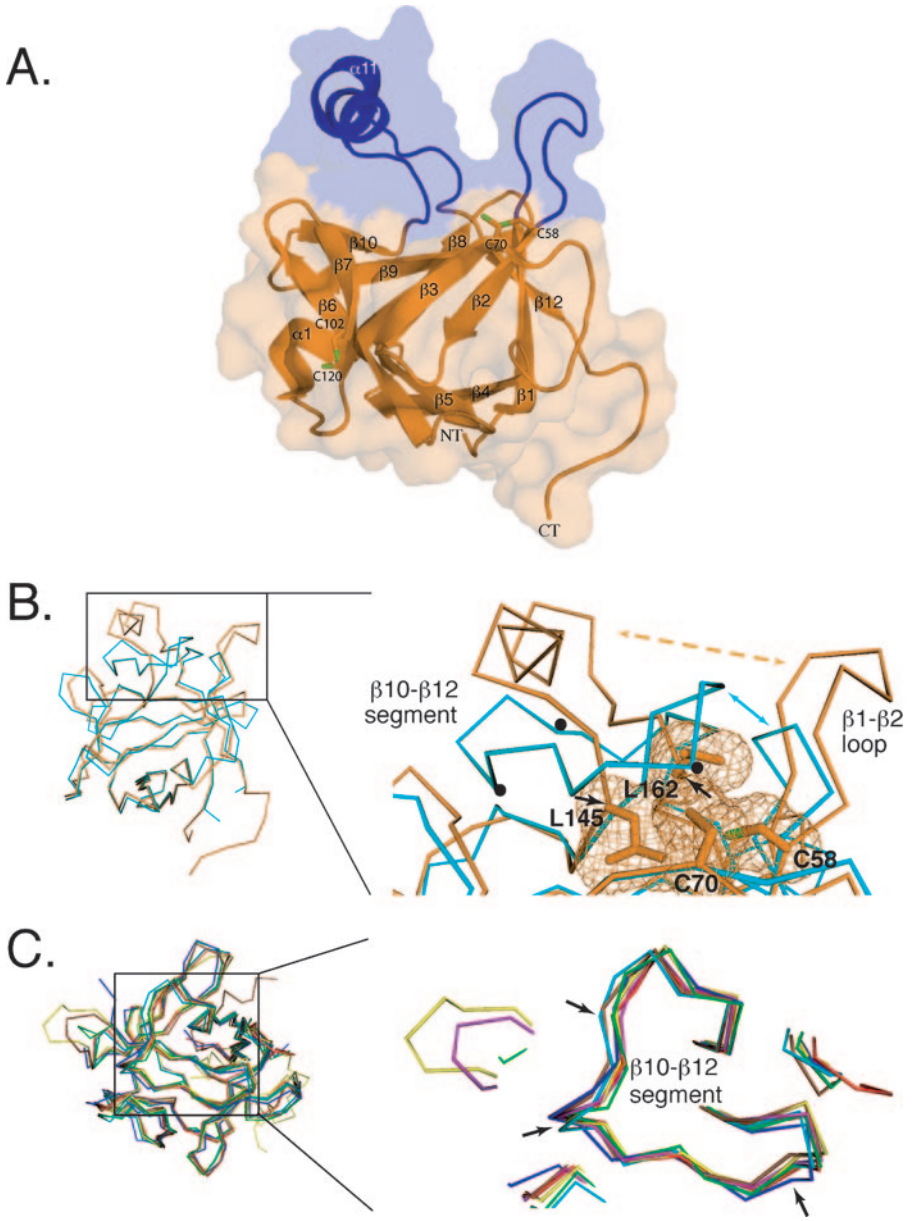

FIG. 2. The HBS topology of FGF19 is completely different from that of classical, paracrine-acting FGFs. (A) Molecular surface and ribbon representation of the FGF19 crystal structure. The molecular surface is shown as transparent. The β strands of FGF19 are labeled according to the conventional strand nomenclature for FGF1 and FGF2. Note that FGF19 lacks the β11 strand present in classical, paracrine-acting FGFs. The HBS, consisting of the loop between β1 and β2 and the segment between β10 and β12, is in blue. A secondary structure element unique to the HBS of FGF19 is the α11 helix located in the β10-β12 segment. Note that α11 and the β1-β2 loop protrude from the β-trefoil like core domain of FGF19 (orange) and that there is a cleft between these two heparin-binding regions. Cysteines 58 (in β2) and 70 (in β3) form a disulfide bridge which stabilizes the altered conformation of the heparin-binding region between β10 and β12 (explained in more detail below). Sulfur atoms are in green. NT and CT, N and C termini of FGF19. (B) Superimposition of the Cα trace of the FGF19 β-trefoil like core onto the Cα trace of the FGF2 β-trefoil from the FGF2-FGFR1c-heparin structure (PDB ID, 1FQ9). A close-up view of the heparin-binding regions is shown on the right, and to aid the reader, a view of the whole structure is shown on the left. FGF19 and FGF2 are in orange and cyan blue, respectively. Black arrowheads mark leucines 145 and 162, at which the Cα trace of FGF19 diverges from that of FGF2 and converges again, respectively. Note that cysteines 58 and 70 of FGF19 form a disulfide bridge which packs against these two leucine residues, thereby stabilizing the altered conformation of the β10-β12 segment. Also note that there are no intramolecular interactions between the β1-β2 loop and the β10-β12 segment in FGF19 (indicated by a dashed orange line with arrowheads; see also the cleft illustrated in panel A), whereas in FGF2, these regions interact with one another (indicated by a cyan blue line with arrowheads). Black circles denote glycine and threonine residues of the GXXXXGXX(T/S) motif present in FGF2 and other classical FGFs (see also panel C). (C) Superimposition of the Cα traces of the β-trefoil core domain of classical, paracrine-acting FGFs onto one another. The view is from the top looking down into the β-trefoil core. A close-up view of the heparin-binding region encompassing β10 and β12 is shown on the right, and to orient the reader, a view of the whole structure is shown on the left. The FGF ligands are colored as follows: FGF1 (PDB ID, 1EVT), green; FGF2 (PDB ID, 1FQ9), cyan blue; FGF4 (PDB ID, 1IJT), red; FGF7 (PDB ID, 1QQL), blue; FGF9 (PDB ID, 1IHK), yellow; FGF10 (PDB ID, 1NUN), purple; and FGF8b (PDB ID, 2FDB), brown. Note that the Cα traces of these seven classical FGFs take nearly identical paths in the β10-β12 region. In panel B, FGF2 was chosen from this set of FGFs to illustrate the divergence of FGF19 at this region. Glycine and threonine/serine residues of the GXXXXGXX(T/S) motif conserved in these classical FGFs are marked by black arrows.

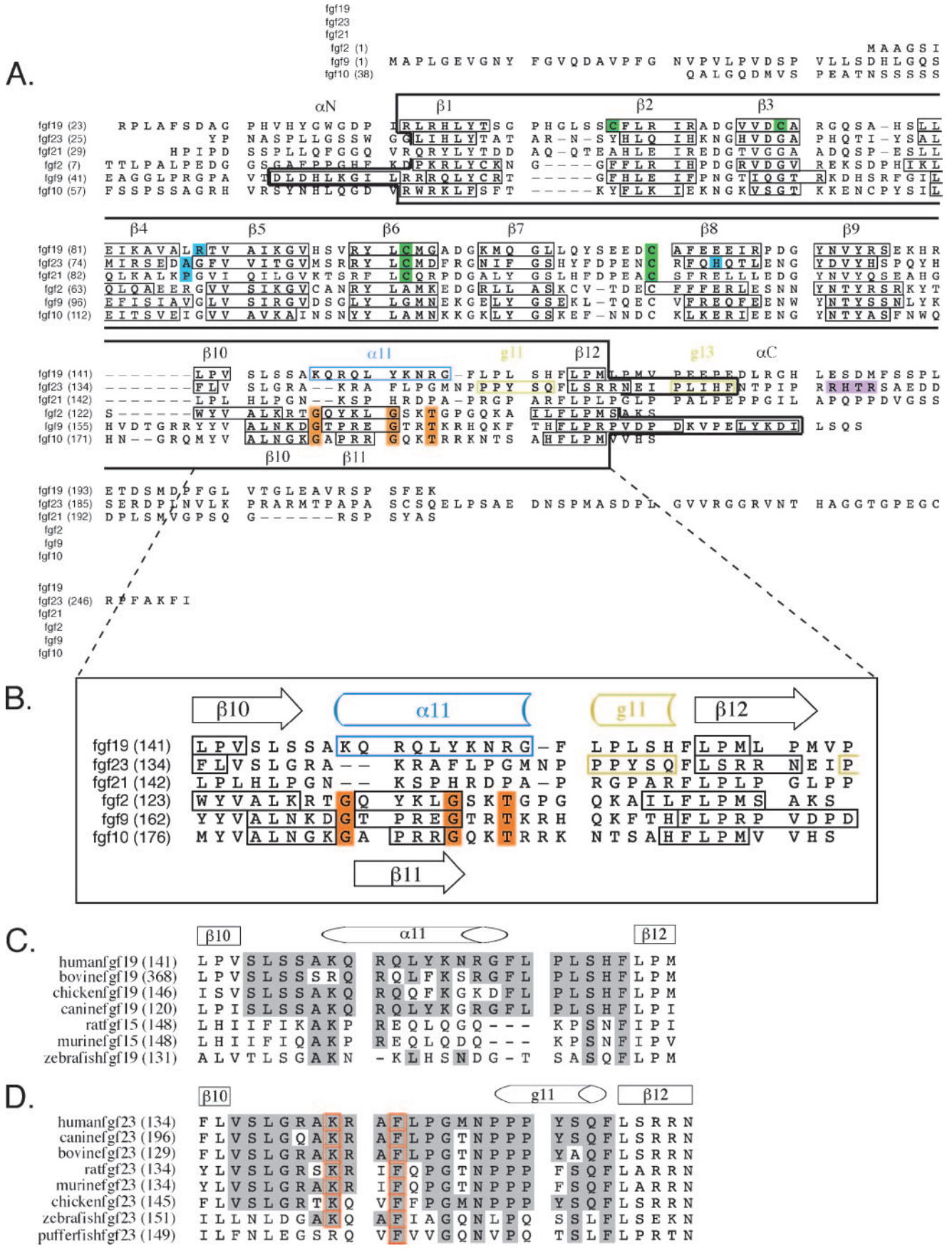
A.
fgf19
fgf23
fgf21
fgf2 (1)
fgf9 (1)
fgf10 (38)
αN
β1
β2
β3
β4
β5
β6
β7
β8
β9
β10
α11
g11
β12
g13
αC
β11
B.
fgf19 (141)
fgf23 (134)
fgf21 (142)
fgf2 (123)
fgf9 (162)
fgf10 (176)
C.
humanfgf19 (141)
bovinefgf19 (368)
chickenfgf19 (146)
caninefgf19 (120)
ratfgf15 (148)
murinefgf15 (148)
zebrafishfgf19 (131)
D.
humanfgf23 (134)
caninefgf23 (196)
bovinefgf23 (129)
ratfgf23 (134)
murinefgf23 (134)
chickenfgf23 (145)
zebrafishfgf23 (151)
pufferfishfgf23 (149)

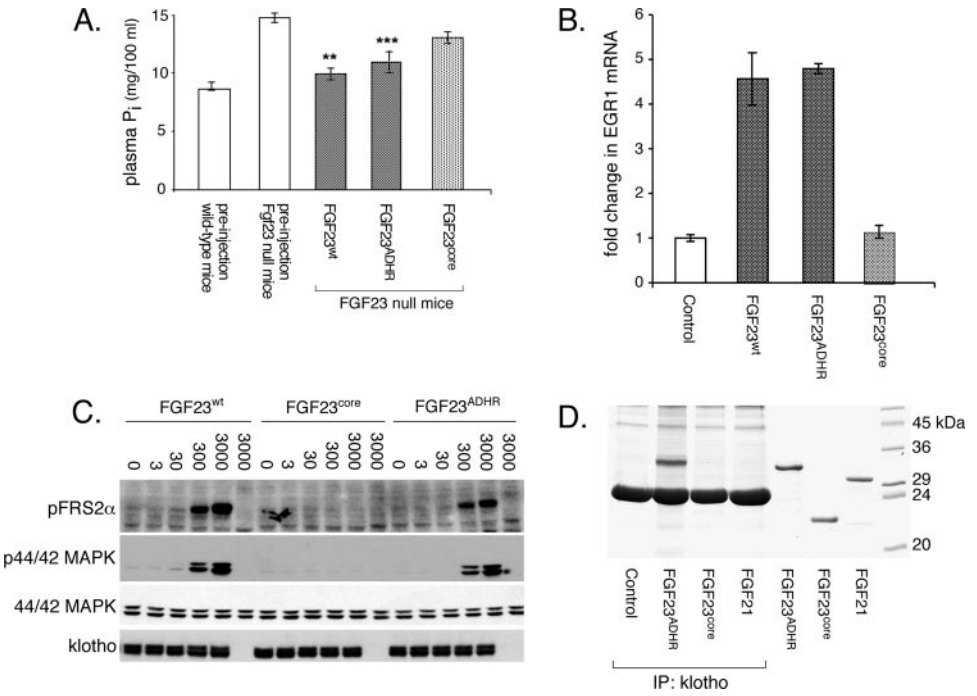

FIG. 4. Recombinant FGF23 protein is biologically active. (A) The unique C-terminal tail of FGF23 is required for phosphaturic activity of FGF23. $FGF23^{wt}$, $FGF23^{ADHR}$, and $FGF23^{core}$ were injected intraperitoneally into *Fgf23*-null mice. Serum phosphate levels were determined before and after protein injection. Note that *Fgf23*-null mice show hyperphosphatemia compared to wild-type mice. (B) The C-terminal tail of FGF23 is required for activation of *EGR1* gene expression by FGF23. HEK293 cells transiently transfected with Klotho were stimulated with $FGF23^{wt}$, $FGF23^{ADHR}$, and $FGF23^{core}$, 1 ng ml^{-1} each, for 30 min. Total RNA was extracted from the cells, and EGR1 mRNA levels were measured by real-time RT-PCR. Data are plotted as change in EGR1 mRNA expression. (C) The C-terminal tail of FGF23 is required for activation of FRS2α and MAP kinase cascade by FGF23. HEK293 cells stably expressing Klotho were stimulated with $FGF23^{wt}$, $FGF23^{ADHR}$, and $FGF23^{core}$, 3 nM to 3 μM each, for 10 min. Cell lysate was prepared and analyzed for phosphorylation of FRS2α (pFRS2α) and 44/42 MAP kinase (p44/42 MAPK) by immunoblotting. Total protein levels of 44/42 MAP kinase and Klotho were measured to control for equal sample loading. (D) The C-terminal tail of FGF23 is required for binding to Klotho. Lysate of HEK293 cells stably expressing Klotho was incubated with $FGF23^{ADHR}$, $FGF23^{core}$, FGF21, or protein sample buffer (control). Klotho was immunoprecipitated from cell lysate (IP) and analyzed for bound FGF proteins.

Efforts to crystallize $FGF23^{wt}$ or $FGF23^{ADHR}$ did not yield crystals, presumably due to the inherent flexibility of the 73-residue C terminus of this ligand. Therefore, we decided to crystallize $FGF23^{core}$, which yielded crystals only in the presence of SOS. These crystals belong to the orthorhombic space group $P2_12_12_1$ and have one FGF23 molecule per asymmetric unit. We solved the crystal structure of $FGF23^{core}$ by molecular replacement using our FGF19 crystal structure as the search model. The β1-β2 loop and the segment between β10 and β12 were omitted from the search model, because of very poor sequence homology. The F_o-F_c difference map showed clear and strong electron density not only for both omitted regions but also for a SOS molecule, allowing us to unambiguously build these heparin-binding regions as well as a SOS molecule bound to these regions. The FGF23-SOS complex structure has been refined to a 1.5-Å resolution with working and free *R* values of 24.3% and 25.5%, respectively (Table 1), and the final model consists of one copy of FGF23 residues 32 to 169 and one SOS molecule (Fig. 5A).

Like FGF19, FGF23 adopts an atypical β-trefoil fold be-

FIG. 3. Structure-based sequence analysis of FGF19 and FGF23. (A) Structure-based sequence alignment of the FGF19 subfamily members and selected paracrine-acting FGFs. Predicted signal sequences have been omitted. Residue numbers are in parentheses on the left of the alignment. Secondary structure elements are given on top of the sequence alignment. The locations and lengths of the secondary structure elements are indicated by boxes in the sequences. A dash in the sequence represents a gap introduced to optimize the alignment. A black box drawn around the sequences marks the boundaries of the β-trefoil core domain for each FGF. Glycine and threonine residues of the GXXXXGXX(T/S) motif are in orange. Note that these residues are conserved among classical, paracrine-acting FGFs but absent in the sequences of the FGF19 subfamily. Residues which, based on published FGF-FGFR structures, likely account for low receptor-binding affinity of FGF19, -21, and -23 are in cyan blue. Cysteine residues forming disulfide bridges are in green. The proteolytic cleavage site motif RXXR in FGF23 is in purple. (B) Close-up view of the sequence alignment of the heparin-binding region encompassing β10 and β12. Sequence labeling is the same as in panel A. (C) Sequence alignment of the heparin-binding β10-β12 region of FGF19 orthologs. Sequence identity to human FGF19 within the β10-β12 region is highlighted in gray. Note the low degree of sequence identity between human FGF19 and rodent and fish orthologs. (D) Sequence alignment of the heparin-binding β10-β12 region of FGF23 orthologs. Sequence labeling is the same as in panel C. Residues critical for the conformation of this region, such as lysine 142 and phenylalanine 145, are indicated by red boxes.

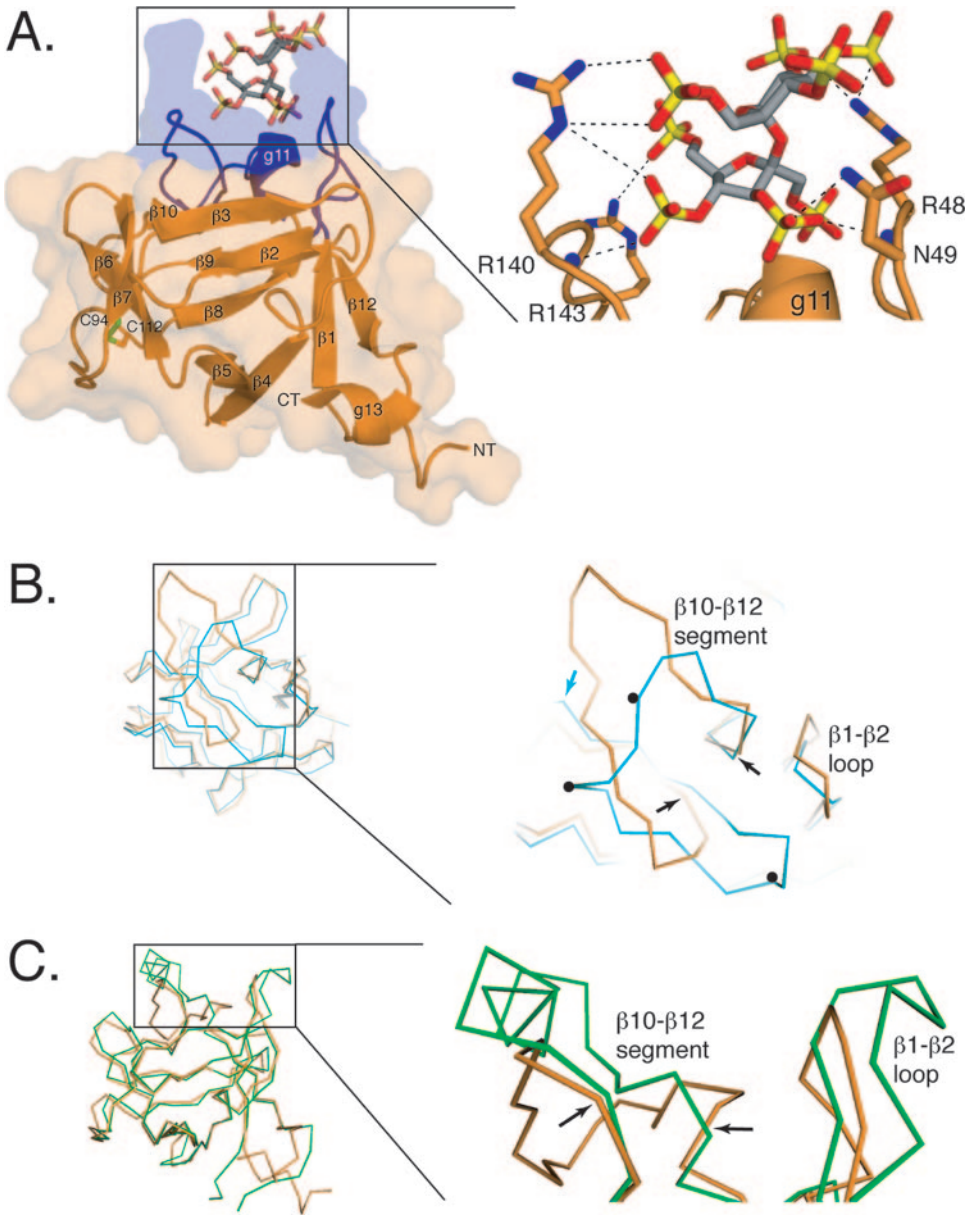

FIG. 5. The HBS topology of FGF23 differs from that of classical, paracrine-acting FGFs and from that of FGF19. (A) Molecular surface and ribbon representation of the crystal structure of the FGF23 core domain in complex with a SOS molecule, shown as sticks. The molecular surface is shown as transparent. A view of the whole structure is shown on the left; a detailed view of the SOS interactions with FGF23 is shown on the right. The β strands of FGF23 are labeled according to the conventional strand nomenclature for FGF1 and FGF2. Note that, like FGF19, FGF23 lacks the β11 strand present in classical, paracrine-acting FGFs. The HBS, consisting of the loop between β1 and β2 and the segment between β10 and β12, is in blue. Note that these regions do not protrude from the β-trefoil like core like those in FGF19 and that the cleft separating these regions from one another is not as prominent as the cleft seen in the FGF19 structure (compare Fig. 2A). A secondary structure element unique to the HBS of FGF23 is the g11 helix, located in the segment between β10 and β12. Also note the C-terminal g13 helix, which is tethered to the core. NT and CT, N and C termini of the FGF23 core domain. The SOS molecule makes hydrogen bonds with arginine 48 and asparagine 49 of the β1-β2 loop and with arginines 140 and 143 of the β10-β12 segment. Note that the sulfated fructose ring of SOS also interacts with backbone atoms of these regions. (B) Superimposition of the Cα trace of the FGF23 β-trefoil like core onto the Cα trace of the FGF2 β-trefoil from the FGF2-FGFR1c-heparin structure (PDB ID, 1FQ9). The viewpoint is from top of the β-trefoil like core. A close-up view of the heparin-binding regions is shown on the right, and to assist the reader, a view of the whole structure is shown on the left. FGF23 and FGF2 are in orange and cyan blue, respectively. Black arrows mark leucine 138 and proline 153, at which the Cα trace of FGF23 diverges from that of FGF2 and converges again, respectively. Glycine and threonine residues of the GXXXXGXX(T/S) motif present in FGF2 and other classical FGFs are labeled with black circles (see also Fig. 2C). The cyan blue arrowhead marks a one-residue insertion in the β9-β10 loop of FGF2 which is sterically incompatible with the conformation of the β10-β12 segment in FGF23. (C) Superimposition of the Cα trace of the FGF23 core domain onto the Cα trace of the FGF19 core. A close-up view of the heparin-binding regions is shown on the right, and to aid the reader, a view of the whole structure is shown on the left. FGF23 and FGF19 are in orange and green, respectively. Black arrows mark glycine 139 and serine 155, at which the Cα trace of FGF23 diverges from that of FGF19 and converges again, respectively. Also note the different β1-β2 loop conformations of FGF23 and FGF19 concurrent with differences in the length of the β1-β2 loop (see Fig. 3A). As in FGF19, there are no intramolecular interactions between the β1-β2 loop and the β10-β12 segment (see also the clefts illustrated in panel A and in Fig. 2A).

cause it also lacks β11. Moreover, the conformation of the segment between β10 and β12 in FGF23 also differs from the canonical conformation of paracrine-acting FGFs (Fig. 5B). The Cα trace of FGF23 diverges from that of paracrine FGFs at exactly the same position as FGF19 does but converges at Pro153, one residue earlier than FGF19 does. Notably, the conformation of the segment between β10 and β12 in the FGF23-SOS complex also differs completely from that of FGF19 (Fig. 5C). The Cα trace of FGF23 diverges from that of FGF19 at Gly139 (homologous to Ser146 in FGF19) and converges again at Ser155, which corresponds to Ser163 in FGF19 (Fig. 3B and 5C). The only secondary structure element assigned to this region by PROCHECK (17) is a g helix (g11) at the C-terminal end of this segment. Additional structural differences between FGF19 and FGF23 are seen at the β1-β2 loop, the other heparin-binding region (Fig. 5C). This is anticipated because FGF23's β1-β2 loop is two residues shorter than that of FGF19 (Fig. 3A). There is also a cleft between the β1-β2 loop and the segment encompassing β10 and β12 (Fig. 5A); this cleft, however, is not as prominent as the one observed in the FGF19 structure.

The β10-β12 region of FGF21 has no sequence identity to FGF19 and only 11% identity to FGF23, and in fact, it is shorter than those of FGF19 and FGF23 (Fig. 3B). This suggests that FGF21 should have yet another HBS topology. The high degree of sequence divergence at this region accounts for the overall low sequence identity among these ligands, as evidenced by the fact that sequence identity is increased to 40 to 45% when these regions are omitted from multiple sequence alignment.

The altered HBS topologies of FGF19 subfamily members are consistent with the lack of the GXXXXGXX(T/S) motif in this subfamily of FGFs. The unconventional conformation of the stretch between β10 and β12 strands observed in our FGF19 and FGF23 structures, and by extension in FGF21, is consistent with the major primary sequence divergence found at this region between FGF19 subfamily members and classical, paracrine-acting FGFs. This region is shorter in FGF19, FGF23, and FGF21 than in paracrine-acting FGFs by one, two, and three residues, respectively, and, most notably, lacks the GXXXXGXX(T/S) motif present in other FGFs (Fig. 3B) (14). The β10-β12 region of reported vertebrate FGF19 and FGF23 orthologs also lacks the GXXXXGXX(T/S) motif (Fig. 3C and D). The FGF19 and FGF23 crystal structures reveal that this sequence motif plays a crucial role in preserving the common conformation of the stretch between β10 and β12 strands among paracrine-acting FGFs. The first glycine from the motif makes hydrogen bonds with a highly conserved glycine in β3, and the second glycine engages in a hydrogen bond with an FGF-invariant glycine in β7. These conserved hydrogen bonds promote formation of β11 and pin down the β10-β12 region to the β-trefoil core. The threonine/serine residue of the GXXXXGXX(T/S) motif, found in 12 of 15 paracrine-acting FGFs, also contributes to the common conformation of the β10-β12 region in these FGFs by forming hydrogen bonds with the second glycine from the motif. However, as is evident from the crystal structure of FGF4, which has a valine instead of the T or S of the motif, those hydrogen bonds are not absolutely required for the observed canonical conformation.

The altered conformation of the β10-β12 region in FGF19 and -23 is consistent with other unique structural features in the vicinity of this region. For example, FGF19 has a cysteine (Cys70) in place of the highly conserved glycine residue in β3 (Fig. 3A). Due to spatial constraints, the presence of a cysteine in this location in FGF19 is incompatible with the canonical conformation of the heparin-binding region seen in paracrine-acting FGFs. It is noteworthy that Cys70 forms a bridge with Cys58 in β2, which facilitates the altered conformation of the region encompassing β10 and β12 in FGF19. Specifically, Leu145 and Leu162, which are positioned at the divergence and convergence points of this region relative to other FGFs, pack against the Cys58-Cys70 disulfide bridge, thereby shielding it against the solvent on one side (Fig. 2B). Hence, visualization of the β10-β12 region in our FGF19 crystal structure shows that this disulfide bridge plays a broader role than merely stabilizing the tertiary structure of FGF19, as initially suggested by Harmer and coworkers (4).

Superimposition of the structurally homologous 11 β strands of FGF23 onto paracrine FGFs shows that the unique conformation of the β10-β12 segment in FGF23 is influenced by structural differences at the β9-β10 loop between this ligand and classical FGFs. FGF19 subfamily members have the shortest β9-β10 loop (Fig. 3A), and structural analysis shows that the longer β9-β10 loop of other FGFs would sterically clash with the conformation of the β10-β12 region observed in the FGF23 structure. Hence, our structural data indicate a previously unrecognized role for the β9-β10 loop in configuring the HBS and may provide an explanation for previously published data showing that mutations in the β9-β10 loop or loop exchange impair FGF biological activity (26).

The altered HBS topology of FGF19/23 is responsible for poor heparin-binding affinity of these FGFs and for their endocrine mode of action. In order to investigate how the altered HBS topology of FGF19/23 would impact the mode of heparin-induced FGFR dimerization by these ligands, we superimposed FGF19/23 onto FGF2-FGFR1c-heparin (PDB ID, 1FQ9) to create 2:2:2 FGF19-FGFR1c-heparin and 2:2:2 FGF23-FGFR1c-heparin dimer models. In each model, the heparin-binding regions sterically clash with sugar backbone and sulfate moieties of the heparin oligosaccharide (Fig. 6). To avoid these steric conflicts, it would be necessary to translate heparin further up from the FGF19/23 core region. The translation of heparin away from FGF19/23 core domains and the presence of a cleft in the HBS of these ligands should translate into poor heparin-binding affinity. This is because the backbone atoms of FGF19/23 would not be able to form hydrogen bonds with *N*-sulfate and 2-*O*-sulfate groups of rings 4 [GlcN(S)6O(S)] and 5 [IdoA(2S)] of heparin; in structures of classical FGFs (e.g., FGF2), backbone atoms of the ligand provide the tightest hydrogen bonds with these two sulfate groups of heparin. The orientation of SOS binding relative to FGF23 is perpendicular to that of heparin binding observed in the FGF23-FGFR-heparin model as well as to that of SOS binding seen in the FGF1-SOS structure (39). This observation further supports our prediction that linear heparin/HS cannot engage the backbone atoms of FGF23. Moreover, FGF23 has a triple proline sequence in this region, which is incapable of making hydrogen bonds with heparin/HS (Fig. 3B).

To test our structural prediction, we used SPR spectroscopy

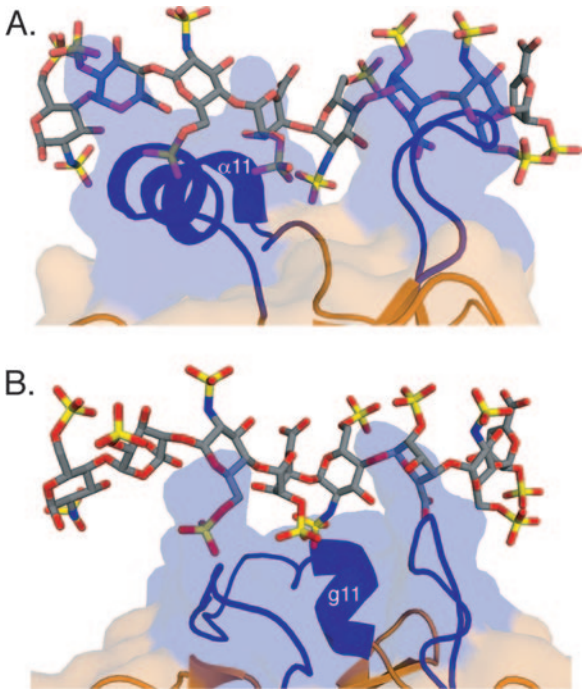

FIG. 6. The HBS topologies of FGF19 and FGF23 impact the mode of heparin binding. (A) Detailed view of heparin binding to FGF19 in a 2:2:2 FGF19-FGFR1c-heparin model created by superimposing FGF19 onto FGF2 in the FGF2-FGFR1c-heparin dimer (PDB ID, 1FQ9). The heparin-binding regions of FGF19 are shown in ribbon and transparent surface representation; the heparin molecule is shown in stick representation. Carbon atoms are in gray, nitrogen atoms are blue, oxygen atoms are red, and sulfur atoms are yellow. Note that there are major steric clashes between the heparin-binding regions of FGF19 and sugar backbone and sulfate groups of the heparin oligosaccharide. A translation of the heparin molecule away from the HBS would be necessary to avoid these clashes, and as a result, the heparin molecule would not be able to interact with backbone atoms of the cleft. (B) Detailed view of heparin binding to FGF23 in a 2:2:2 FGF23-FGFR1c-heparin model created by superimposing the FGF23 core domain onto FGF2 in the FGF2-FGFR1c-heparin dimer (PDB ID, 1FQ9). Representation of the heparin-binding regions of FGF23 and the heparin oligosaccharide, and atom coloring are the same as in panel A. Note that the heparin-binding regions of FGF23 also sterically clash with sugar backbone and sulfate groups of the heparin molecule, although not to the extent as seen in the FGF19-heparin model (compare panels A and B).

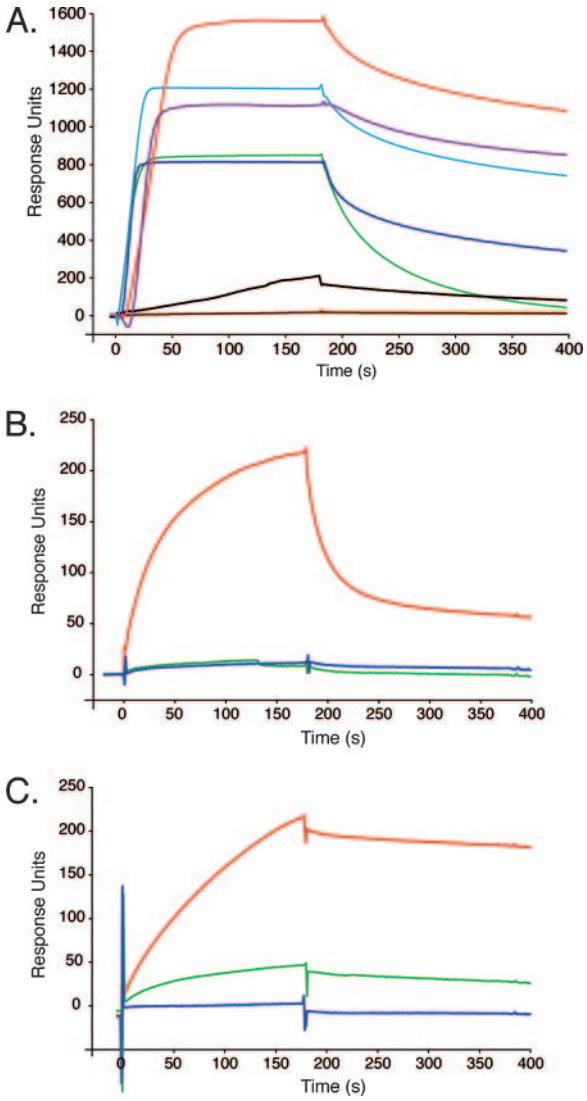

FIG. 7. FGF19 subfamily members exhibit unusually low binding affinity for heparin, and structure-based mutagenesis identifies residues engaged in heparin binding in FGF19 and FGF23. (A) Representative SPR sensorgram of heparin binding of FGF19 (orange), FGF21 (brown), FGF23 (black), FGF10 (purple), FGF7 (blue), FGF4 (red), FGF2 (cyan blue) and FGF1 (green), 100 nM each. (B) Representative SPR sensorgram of heparin-binding of wild-type FGF19 (red) and FGF19 HBS mutants, $FGF19^{K149A}$ (blue) and $FGF19^{K149A,R157A}$ (green), 800 nM each. (C) SPR sensorgram illustrating heparin-binding of HBS mutants of FGF23, $FGF23^{R48,N49}$ (green), and $FGF23^{R140,R143}$ (blue), 800 nM each. The mutations were introduced into the ADHR mutant of FGF23 (red). FGF-heparin binding was studied at 25°C. The biosensor chip response is plotted as a function of time.

to compare heparin binding of FGF19, -21, and -23 with that of paracrine-acting FGFs, including FGF1, FGF2, FGF4, FGF7, and FGF10. In support of our structural prediction, the SPR data show that FGF19, -21, and -23 bind poorly to heparin (Fig. 7A). Importantly, the poor binding affinities of FGF19, -21, and -23 for heparin are in keeping with the endocrine behavior of FGF19 subfamily members. The poor heparin-binding affinity should allow FGF19 subfamily members to escape the pericellular HS of the tissues where they are produced. Owing to their high affinity for heparin/HS, however, paracrine-acting FGFs are entrapped in the pericellular environment of tissues at or near the site of their synthesis and release, and these FGFs can diffuse over a short range only, locally within tissues.

The FGF19-FGFR-heparin model suggested that Lys149, Gln152, Lys155, Asn156, and Arg157 of the β10-β12 segment and His53 of the β1-β2 loop bind heparin in FGF19 because these residues are in the vicinity of the heparin oligosaccharide. To test this hypothesis, we mutated Lys149 and Arg157 alone and in combination with alanine. SPR analysis shows that these mutations impair the ability of FGF19 to bind heparin (Fig. 7B). In the FGF23-SOS structure, SOS binds with its sulfated fructose ring facing into the cleft (Fig. 5A). Arg48, Asn49, Arg140, and Arg143 of FGF23 coordinate four differ-

ent sulfates of SOS, suggesting that these are potential heparin-binding residues in this ligand (Fig. 5A). To test whether these SOS-coordinating residues of FGF23 are indeed engaged in heparin binding, we introduced two double mutations into FGF23 (R48A-N49A and R140A-R143A). SPR analysis shows that these FGF23 mutants failed to bind heparin (Fig. 7C), providing experimental evidence for the unique HBS topology seen in the crystal structure of FGF23.

Concluding remarks. The requirement for HS is universal for signaling by all FGFs. While conferring endocrine ability to FGF19 subfamily members, the poor heparin-binding affinity of these ligands will reduce the ability of HS/heparin to promote binding of these ligands to their cognate FGFR and hence should negatively impact signaling by these FGFs. Modeling studies reveal that in each of the three FGF19 subfamily members, a predicted key residue for FGFR binding is replaced, so that these FGFs have inherently low affinity for their cognate receptors (Fig. 3A). The low receptor-binding affinity together with the low HS/heparin-binding affinity of these FGFs is the molecular basis for the dependence of these ligands on Klotho proteins to signal in their target tissues. By simultaneously interacting with FGF19, -21, and -23 and their cognate FGFRs, Klotho/βKlotho bring about binding affinity that is just sufficient to produce a metabolic but not mitogenic response. The restricted expression of Klotho proteins also contributes to the endocrine behavior of FGF19, -21, and -23 by limiting the signaling of these ligands to specific tissues. In addition to providing molecular insights into the endocrine mode of action of the FGF19 subfamily, our structural data may also provide blueprints for rational drug design for metabolic syndromes, such as diabetes, obesity, and hypercholesterolemia, as well as disordered phosphate and vitamin D homeostasis.

ACKNOWLEDGMENTS

This work was supported by grants from the National Institutes of Health (DE13686 to M.M.; DK063934 to K.W.; AG19712 and AG25326 to M.K.; HL62244, HL52622, and GM38060-17 to R.L.; DK067158 to S.K.; S10 RR017990 to T.N.), the Irma T. Hirschl Fund (to M.M.), the Robert A. Welch Foundation (to S.K.), the Eisai Research Fund (to M.K.), and the Ellison Medical Foundation (to M.K.) and by institutional support from Harvard School of Dental Medicine (to B.L. and M.S.R.). We are grateful to H. C. Deitz and D. E. Arking for providing Klotho cDNA (to K.W.).

We are grateful to R. Abramowitz and J. Schwanof for assistance at beam line X4A at the National Synchrotron Light Source, a DOE facility. Beam line X4A is supported by the New York Structural Biology Center.

REFERENCES

1. **Araya, K., S. Fukumoto, R. Backenroth, Y. Takeuchi, K. Nakayama, N. Ito, N. Yoshii, Y. Yamazaki, T. Yamashita, J. Silver, T. Igarashi, and T. Fujita.** 2005. A novel mutation in fibroblast growth factor 23 gene as a cause of tumoral calcinosis. J. Clin. Endocrinol Metab. **90:**5523–5527.
2. **Bellosta, P., A. Iwahori, A. N. Plotnikov, A. V. Eliseenkova, C. Basilico, and M. Mohammadi.** 2001. Identification of receptor and heparin binding sites in fibroblast growth factor 4 by structure-based mutagenesis. Mol. Cell. Biol. **21:**5946–5957.
3. **Bottcher, R. T., and C. Niehrs.** 2005. Fibroblast growth factor signaling during early vertebrate development. Endocr. Rev. **26:**63–77.
4. **Harmer, N. J., L. Pellegrini, D. Chirgadze, J. Fernandez-Recio, and T. L. Blundell.** 2004. The crystal structure of fibroblast growth factor (FGF) 19 reveals novel features of the FGF family and offers a structural basis for its unusual receptor affinity. Biochemistry **43:**629–640.
5. **Holt, J. A., G. Luo, A. N. Billin, J. Bisi, Y. Y. McNeill, K. F. Kozarsky, M. Donahee, Y. Wang da, T. A. Mansfield, S. A. Kliewer, B. Goodwin, and S. A. Jones.** 2003. Definition of a novel growth factor-dependent signal cascade for the suppression of bile acid biosynthesis. Genes Dev. **17:**1581–1591.
6. **Ibrahimi, O. A., F. Zhang, A. V. Eliseenkova, N. Itoh, R. J. Linhardt, and M. Mohammadi.** 2004. Biochemical analysis of pathogenic ligand-dependent FGFR2 mutations suggests distinct pathophysiological mechanisms for craniofacial and limb abnormalities. Hum. Mol. Genet. **13:**2313–2324.
7. **Ibrahimi, O. A., F. Zhang, S. C. Hrstka, M. Mohammadi, and R. J. Linhardt.** 2004. Kinetic model for FGF, FGFR, and proteoglycan signal transduction complex assembly. Biochemistry **43:**4724–4730.
8. **Inagaki, T., M. Choi, A. Moschetta, L. Peng, C. L. Cummins, J. G. McDonald, G. Luo, S. A. Jones, B. Goodwin, J. A. Richardson, R. D. Gerard, J. J. Repa, D. J. Mangelsdorf, and S. A. Kliewer.** 2005. Fibroblast growth factor 15 functions as an enterohepatic signal to regulate bile acid homeostasis. Cell Metab. **2:**217–225.
9. **Ito, S., T. Fujimori, A. Furuya, J. Satoh, Y. Nabeshima, and Y. Nabeshima.** 2005. Impaired negative feedback suppression of bile acid synthesis in mice lacking βKlotho. J. Clin. Investig. **115:**2202–2208.
10. **Kharitonenkov, A., T. L. Shiyanova, A. Koester, A. M. Ford, R. Micanovic, E. J. Galbreath, G. E. Sandusky, L. J. Hammond, J. S. Moyers, R. A. Owens, J. Gromada, J. T. Brozinick, E. D. Hawkins, V. J. Wroblewski, D. S. Li, F. Mehrbod, S. R. Jaskunas, and A. B. Shanafelt.** 2005. FGF-21 as a novel metabolic regulator. J. Clin. Investig. **115:**1627–1635.
11. **Kuro-o, M., Y. Matsumura, H. Aizawa, H. Kawaguchi, T. Suga, T. Utsugi, Y. Ohyama, M. Kurabayashi, T. Kaname, E. Kume, H. Iwasaki, A. Iida, T. Shiraki-Iida, S. Nishikawa, R. Nagai, and Y. I. Nabeshima.** 1997. Mutation of the mouse klotho gene leads to a syndrome resembling ageing. Nature **390:**45–51.
12. **Kurosu, H., Y. Ogawa, M. Miyoshi, M. Yamamoto, A. Nandi, K. P. Rosenblatt, M. G. Baum, S. Schiavi, M. C. Hu, O. W. Moe, and M. Kuro-o.** 2006. Regulation of fibroblast growth factor-23 signaling by klotho. J. Biol. Chem. **281:**6120–6123.
13. **Lundasen, T., C. Galman, B. Angelin, and M. Rudling.** 2006. Circulating intestinal fibroblast growth factor 19 has a pronounced diurnal variation and modulates hepatic bile acid synthesis in man. J. Intern. Med. **260:**530–536.
14. **Luo, Y., W. Lu, K. A. Mohamedali, J. H. Jang, R. B. Jones, J. L. Gabriel, M. Kan, and W. L. McKeehan.** 1998. The glycine box: a determinant of specificity for fibroblast growth factor. Biochemistry **37:**16506–16515.
15. **Mohammadi, M., S. K. Olsen, and R. Goetz.** 2005. A protein canyon in the FGF-FGF receptor dimer selects from an a la carte menu of heparan sulfate motifs. Curr. Opin. Struct. Biol. **15:**506–516.
16. **Mohammadi, M., S. K. Olsen, and O. A. Ibrahimi.** 2005. Structural basis for fibroblast growth factor receptor activation. Cytokine Growth Factor Rev. **16:**107–137.
17. **Morris, A. L., M. W. MacArthur, E. G. Hutchinson, and J. M. Thornton.** 1992. Stereochemical quality of protein structure coordinates. Proteins **12:** 345–364.
18. **Murzin, A. G., A. M. Lesk, and C. Chothia.** 1992. beta-Trefoil fold. Patterns of structure and sequence in the Kunitz inhibitors interleukins-1 beta and 1 alpha and fibroblast growth factors. J. Mol. Biol. **223:**531–543.
19. **National Research Council.** 1996. Guide for the care and use of laboratory animals. National Academy Press, Washington, DC.
20. **Olsen, S. K., J. Y. Li, C. Bromleigh, A. V. Eliseenkova, O. A. Ibrahimi, Z. Lao, F. Zhang, R. J. Linhardt, A. L. Joyner, and M. Mohammadi.** 2006. Structural basis by which alternative splicing modulates the organizer activity of FGF8 in the brain. Genes Dev. **20:**185–198.
21. **Ornitz, D. M., and N. Itoh.** 2001. Fibroblast growth factors. Genome Biol. **2:**reviews3005.1-reviews3005.12.
22. **Plotnikov, A. N., A. V. Eliseenkova, O. A. Ibrahimi, Z. Shriver, R. Sasisekharan, M. A. Lemmon, and M. Mohammadi.** 2001. Crystal structure of fibroblast growth factor 9 reveals regions implicated in dimerization and autoinhibition. J. Biol. Chem. **276:**4322–4329.
23. **Plotnikov, A. N., S. R. Hubbard, J. Schlessinger, and M. Mohammadi.** 2000. Crystal structures of two FGF-FGFR complexes reveal the determinants of ligand-receptor specificity. Cell **101:**413–424.
24. **Razzaque, M. S., D. Sitara, T. Taguchi, R. St-Arnaud, and B. Lanske.** 2006. Premature aging-like phenotype in fibroblast growth factor 23 null mice is a vitamin D-mediated process. FASEB J. **20:**720–722.
25. **Schlessinger, J., A. N. Plotnikov, O. A. Ibrahimi, A. V. Eliseenkova, B. K. Yeh, A. Yayon, R. J. Linhardt, and M. Mohammadi.** 2000. Crystal structure of a ternary FGF-FGFR-heparin complex reveals a dual role for heparin in FGFR binding and dimerization. Mol. Cell **6:**743–750.
26. **Sher, I., A. Weizman, S. Lubinsky-Mink, T. Lang, N. Adir, D. Schomburg, and D. Ron.** 1999. Mutations uncouple human fibroblast growth factor (FGF)-7 biological activity and receptor binding and support broad specificity in the secondary receptor binding site of FGFs. J. Biol. Chem. **274:** 35016–35022.
27. **Shimada, T., M. Kakitani, Y. Yamazaki, H. Hasegawa, Y. Takeuchi, T. Fujita, S. Fukumoto, K. Tomizuka, and T. Yamashita.** 2004. Targeted ablation of Fgf23 demonstrates an essential physiological role of FGF23 in phosphate and vitamin D metabolism. J. Clin. Investig. **113:**561–568.
28. **Shimada, T., T. Muto, I. Urakawa, T. Yoneya, Y. Yamazaki, K. Okawa, Y. Takeuchi, T. Fujita, S. Fukumoto, and T. Yamashita.** 2002. Mutant FGF-23

responsible for autosomal dominant hypophosphatemic rickets is resistant to proteolytic cleavage and causes hypophosphatemia in vivo. Endocrinology **143:**3179–3182.

29. **Sitara, D., M. S. Razzaque, M. Hesse, S. Yoganathan, T. Taguchi, R. G. Erben, H. Juppner, and B. Lanske.** 2004. Homozygous ablation of fibroblast growth factor-23 results in hyperphosphatemia and impaired skeletogenesis, and reverses hypophosphatemia in Phex-deficient mice. Matrix Biol. **23:**421–432.
30. **Thisse, B., and C. Thisse.** 2005. Functions and regulations of fibroblast growth factor signaling during embryonic development. Dev. Biol. **287:**390–402.
31. **Tohyama, O., A. Imura, A. Iwano, J. N. Freund, B. Henrissat, T. Fujimori, and Y. Nabeshima.** 2004. Klotho is a novel beta-glucuronidase capable of hydrolyzing steroid beta-glucuronides. J. Biol. Chem. **279:**9777–9784.
32. **Tomlinson, E., L. Fu, L. John, B. Hultgren, X. Huang, M. Renz, J. P. Stephan, S. P. Tsai, L. Powell-Braxton, D. French, and T. A. Stewart.** 2002. Transgenic mice expressing human fibroblast growth factor-19 display increased metabolic rate and decreased adiposity. Endocrinology **143:**1741–1747.
33. **Urakawa, I., Y. Yamazaki, T. Shimada, K. Iijima, H. Hasegawa, K. Okawa, T. Fujita, S. Fukumoto, and T. Yamashita.** 2006. Klotho converts canonical FGF receptor into a specific receptor for FGF23. Nature.
34. **White, K. E., W. E. Evans, J. L. H. O'Riordan, M. C. Speer, M. J. Econs, B. Lorenz-Depiereux, M. Grabowski, T. Meitinger, and T. M. Strom.** 2000. Autosomal dominant hypophosphataemic rickets is associated with mutations in FGF23. Nat. Genet. **26:**345–348.
35. **White, K. E., G. Carn, B. Lorenz-Depiereux, A. Benet-Pages, T. M. Strom, and M. J. Econs.** 2001. Autosomal-dominant hypophosphatemic rickets (ADHR) mutations stabilize FGF-23. Kidney Int. **60:**2079–2086.
36. **Yamazaki, Y., R. Okazaki, M. Shibata, Y. Hasegawa, K. Satoh, T. Tajima, Y. Takeuchi, T. Fujita, K. Nakahara, T. Yamashita, and S. Fukumoto.** 2002. Increased circulatory level of biologically active full-length FGF-23 in patients with hypophosphatemic rickets/osteomalacia. J. Clin. Endocrinol. Metab. **87:**4957–4960.
37. **Ye, S., Y. Luo, W. Lu, R. B. Jones, R. J. Linhardt, I. Capila, T. Toida, M. Kan, H. Pelletier, and W. L. McKeehan.** 2001. Structural basis for interaction of FGF-1, FGF-2, and FGF-7 with different heparan sulfate motifs. Biochemistry **40:**14429–14439.
38. **Yeh, B. K., M. Igarashi, A. V. Eliseenkova, A. N. Plotnikov, I. Sher, D. Ron, S. A. Aaronson, and M. Mohammadi.** 2003. Structural basis by which alternative splicing confers specificity in fibroblast growth factor receptors. Proc. Natl. Acad. Sci. USA **100:**2266–2271.
39. **Zhu, X., B. T. Hsu, and D. C. Rees.** 1993. Structural studies of the binding of the anti-ulcer drug sucrose octasulfate to acidic fibroblast growth factor. Structure **1:**27–34.
40. **Zhu, X., H. Komiya, A. Chirino, S. Faham, G. M. Fox, T. Arakawa, B. T. Hsu, and D. C. Rees.** 1991. Three-dimensional structures of acidic and basic fibroblast growth factors. Science **251:**90–93.